

**A Method to Retrieve Rainfall Rate over Land from TRMM Microwave Imager
Observations**

C. Prabhakara¹, R. Iacovazzi, Jr.², and J.-M. Yoo³

¹NASA/Goddard Space Flight Center, Greenbelt, MD

²Science Systems and Applications, Inc., Lanham, MD

³EWHA Womans University, Seoul, South Korea

Journal of Geophysical Research

Corresponding Author Address:

C. Prabhakara

NASA/Goddard Space Flight Center, Code 913

Greenbelt, Maryland 20771

Phone : 301-614-6193; Fax : 301-614-6307; E-mail : cuddapah@climate.gsfc.nasa.gov

A Method to Retrieve Rainfall Rate over land from TRMM Observations

C. Prabhakara¹, R. Iacovazzi, Jr.², and J.-M. Yoo³

Submitted to Journal of Geophysical Research

Retrieving rain rate on land with the help of the Tropical Rainfall Measuring Mission (TRMM) Microwave Imager (TMI) radiometer data is difficult because of the highly variable nature of the land surface. By developing a theoretical link between the observations of this passive radiometer and the measurements of the Precipitation Radar (PR) onboard the TRMM satellite, we are able to derive relationships between the TMI and PR observations. These relationships permit us to retrieve rain rate from intense and decaying thunderstorms, as well as the areas away from such features. This radiometer rain rate estimation method shows a good correlation with the radar rain rate observations over areas on the order of 200 km x 200 km, as well as on much finer spatial scales (~20 km x 20 km). In the absence of a satellite-borne radar, this technique is useful to obtain the rain information from the passive microwave radiometer.

¹NASA/Goddard Space Flight Center, Greenbelt, MD

²SSAI, Lanham, MD

³ EWha Womans University, Seoul, South Korea

Abstract: Over tropical land regions, rain rate maxima in mesoscale convective systems revealed by the Precipitation Radar (PR) flown on the Tropical Rainfall Measuring Mission (TRMM) satellite are found to correspond to thunderstorms, i.e., Cbs. These Cbs are reflected as minima in the 85 GHz brightness temperature, T85, observed by the TRMM Microwave Imager (TMI) radiometer. Because the magnitude of TMI observations do not discriminate satisfactorily convective and stratiform rain, we developed here a different TMI discrimination method. In this method, two types of Cbs, strong and weak, are inferred from the Laplacian of T85 at minima. Then, to retrieve rain rate, where T85 is less than 270 K, a weak (background) rain rate is deduced using T85 observations. Furthermore, over a circular area of 10 km radius centered at the location of each T85 minimum, an additional Cb component of rain rate is added to the background rain rate. This Cb component of rain rate is estimated with the help of (T19-T37) and T85 observations. Initially, our algorithm is calibrated with the PR rain rate measurements from 20 MCS rain events. After calibration, this method is applied to TMI data taken from several tropical land regions. With the help of the PR observations, we show that the spatial distribution and intensity of rain rate over land estimated from our algorithm are better than those given by the current TMI-Version-5 Algorithm. For this reason, our algorithm may be used to improve the current state of rain retrievals on land.

1. Introduction

Rain rate is highly variable in space and time. Because of this, measuring rain rate globally with the help of remote sensors becomes a challenging problem. Ground-based radars have been extensively used to sense rain, and they have provided considerable insight into the nature of hydrometeors over limited regions. In the recent Tropical Rainfall Measuring Mission¹ (TRMM), the satellite-borne Precipitation Radar (PR) and TRMM Microwave Imager (TMI) radiometer have been flown together on a satellite to estimate rain rate over the entire tropics. In the forthcoming Global Precipitation Measurement (GPM) mission, microwave radiometers will be flown on a constellation of satellites to take into account the diurnal variability of rain rate over the globe (E. A. Smith, personal communication). However, as a benchmark, only one of these GPM satellites will contain a precipitation radar. So, it is necessary to have a microwave radiometer rain retrieval technique that can be used in the absence of supporting information given by a precipitation radar.

Satellite-borne precipitation radar is an active remote sensing device that can give the profile of reflectivity in the atmosphere with a fine vertical resolution. After correcting radar reflectivity for attenuation, one can infer the rain rate near the surface and the vertical profile of hydrometeors in a column of the atmosphere (Iguchi et al., 2000). It may be noted that in this procedure, the hydrometeor particle size distribution (PSD) is assumed. Also, the data from the satellite precipitation radar can be utilized to discriminate convective and stratiform rain regions. On the other hand, the brightness temperature (T_b) observations made by a satellite-borne passive microwave radiometer lack some of the above properties. Radiometer observations depend on the absorption, emission, and scattering properties of the constituents in an entire column of the

¹ Tropical Rainfall Measuring Mission: A satellite mission launched in November 1997 to quantify tropical rainfall and atmospheric latent heating (see Simpson et al., 1996). Onboard the TRMM satellite, there is the conical-scanning TRMM Microwave Imager radiometer that has dual-polarization channels at 10.7, 19.3, 37, and 85.5 GHz and a vertical-polarization channel at about 21 GHz. In addition, there is the cross-track-scanning Precipitation Radar that operates at a frequency of 13.8 GHz

atmosphere. Thus, estimates of near-surface rain rate from the radiometer data are generally contaminated by all other hydrometeors in a vertical column of the atmosphere.

For the purpose of retrieving rain rate from microwave radiometers, Kummerow et al. (1989) developed an algorithm that utilizes results obtained from a numerical cloud resolving model (CRM). Using the CRM, information about the vertical profile of hydrometeors and surface rain rate is generated for footprint-sized regions (~10 km). For each profile of CRM generated hydrometeors, a set of Tbs - i.e., T85, T37, T21, T19, and T10 - are simulated using a radiative transfer model. These hydrometeor profiles, and the corresponding sets of simulated Tbs, serve as a lookup table. Given a set of observed Tbs from a microwave radiometer, one can in principle match to these Tbs a suitable hydrometeor profile and corresponding rain rate based on the information in the lookup table. Kummerow et al. (1989) used a multiple regression technique to perform such matching. In a later study, Kummerow et al. (1996) replaced this matching technique with a Bayesian statistical procedure. In general, for a given set of observed Tbs, there can be a significant diversity in the hydrometeor profiles that can be matched from the lookup table. So, to obtain an acceptable hydrometeor profile and rain rate, additional a priori constraints are included in this matching procedure (Kummerow, 2001). These constraints depend upon the limitations of the CRM and radiative transfer models.

An important consideration in microwave radiometer rain retrieval methods is the relationship between rain rate and scattering of microwave radiation by ice particles. However, Schols et al. (1999) show that this scattering depends on the density of ice particles. From a theoretical simulation study, Prabhakara et al. (2002) show that knowledge of the vertical distribution of the density, and also the phase, of hydrometeors is necessary in order to differentiate convective rain from stratiform rain. Unfortunately, the density and the vertical distribution of hydrometeors cannot be determined from the magnitude and polarization of microwave radiometer

brightness temperatures. As a result, microwave radiometers fail to differentiate satisfactorily convective rain from stratiform rain. This can lead to significant errors in rain retrievals.

In order to overcome this weakness, in the rain retrieval methods of Olson et al. (1999), Hong et al. (1999), and Kummerow et al. (2001), information deduced from the spatial gradient of the brightness temperatures and/or polarization in the 85 GHz measurements is used to estimate a convective rain fraction in each radiometer footprint. This procedure is tuned empirically with the observations of a radar. Apparently, this retrieval method does not work over land (Kummerow et al., 2001). For this reason, to retrieve rain rate on land, Kummerow et al. modified their method to incorporate the concepts of a multiple regression technique developed by Grody et al. (1991). This radiometer rain retrieval method constitutes the current Version 5 TRMM algorithm to estimate rain rate from TMI data over land. In this study, we will address this retrieval method as the TMI-Version-5 (TMI-V5 from hereafter) Algorithm.

In an alternate approach, using microwave radiometer data Prabhakara et al. (2000 - hereafter PIWD) developed a rain retrieval model that can be calibrated with the rain rate derived from PR. This method takes advantage of the fact that there is a theoretical link between rain rate and Tbs observed by a microwave radiometer (e.g., Wu and Weinman, 1984). In the study of PIWD, the information obtained from the spatial distribution of Tbs is used differently. A local minimum in the 85 GHz observed by TMI is used to identify the presence of a thunderstorm, or Cb. At the location of each minimum, the Laplacian of T85, $\nabla^2 T85$, is computed. Then, the magnitude of this Laplacian is used to categorize each Cb as weak or strong. With the help of these Cbs, PIWD showed that it is possible to estimate rain rate over both land and ocean satisfactorily.

Over land areas, rain retrieval from microwave radiometer data is complicated by terrain and also by changes in surface emissivity produced by soil type, vegetation, and soil moisture (e.g., Conner and Petty, 1998). In addition, the microwave signal in the long wavelength channels

representing emission from rain drops is greatly diminished, because of reduced contrast between the temperature of dry land and the rain clouds. Recognizing these problems, our goal in this study is to improve the TMI-V5 Algorithm over land.

2. Comparison of TMI and PR Observations Pertaining to Rain Over Tropical Land

In convection, rain drops grow by the collision-coalescence mechanism primarily below the freezing level. Above the freezing level, the relatively strong vertical motions lead to a layer containing particles of water and ice in mixed-phased form (see Smith et al., 1999; Bringi et al., 1997; Balakrishnan and Zrnica, 1990; and Sax and Keller, 1980). The typical scale of convective cells (~ 2 km) leads to appreciable horizontal variability in radar reflectivity factor, Z (hereafter termed reflectivity), measurements in the convective regime.

In stratiform rain regions, the growth of hydrometeors takes place mainly above the freezing level, and is due to deposition of water vapor onto slowly-falling ice particles that form large, low-density ice aggregates (snow flakes) (see Houze, 1997). Below the freezing level, snow flakes melt within about a distance of 500 m. Under favorable conditions, this melting layer manifests itself as a "bright band", or peak, in the radar reflectivity profile. Furthermore, radar reflectivity measurements show that there is a relatively uniform distribution of hydrometeors in the horizontal.

From the above discussion, it follows that the presence of a bright band in the vertical profile of Z and/or horizontal variability of Z leads to inference of rain type from radar data. Such robust information is missing in the microwave radiometer observations. For this reason, using the rain type classification of PR, we have partitioned subjectively the nearly simultaneously TMI data taken over rain scenes in tropical land areas into convective and stratiform categories. These partitioned TMI data can be analyzed with the help of the vertical profile of reflectivity and near-

surface rate given by PR to gain a better insight into the microwave radiometer observations, and thereby help improve rain retrieval from TMI.

2.A. Maps and Cross-Sections

The near-surface rain rate deduced from PR observations has a horizontal resolution of about 4.3 km x 4.3 km. The satellite observations of PR are arranged uniformly at a spacing of about 4.3 km both along and across scan lines. On the other hand, the footprints of the TMI 85 GHz (vertical and horizontal polarization channels) are approximately 5.0 km x 7.0 km. These footprints are separated by about 5.0 km along conical scan lines and about 14 km across scan lines. This scan pattern of TMI degrades the effective resolution of the 85 GHz channel compared to that of the PR. The TMI radiometer contains additional channels in vertical and horizontal polarization near 10, 19, and 37 GHz that have a resolution of about 40, 20, and 10 km, respectively. Furthermore, TMI has a 21 GHz channel in vertical polarization that has a resolution similar to that of 19 GHz. In this study, we are scrutinizing the information given by the PR and the TMI in the 19, 37, and 85 GHz channels. The TMI 10 and 21 GHz channels are not included in this investigation. This is because the 10 GHz channel has a relatively large footprint, and the information given by the 21 GHz channel is very similar to that of 19 GHz. Also, we consider only the vertical polarization measurements made by TMI, because they are affected less by the surface emissivity. Note, for simplicity that all Tbs indicated from hereafter represent vertical polarization.

In Figures 1a-e, we show respectively maps of T19, T37, (T19-T37), and T85, as well as a map of PR near-surface rain rate, for a mesoscale convective system (MCS) that occurred over the Southeast United States on 5 June 1998. From these figures, we note that the spatial pattern of PR rain rate compares well with that of T85, but not with that of T19 or T37. We find in the map of T85 that there are localized minima with a scale of about 10 to 20 km. In Figure 1f, the locations of these minima in T85 for this MCS are indicated with the letters S and w. These minima in T85

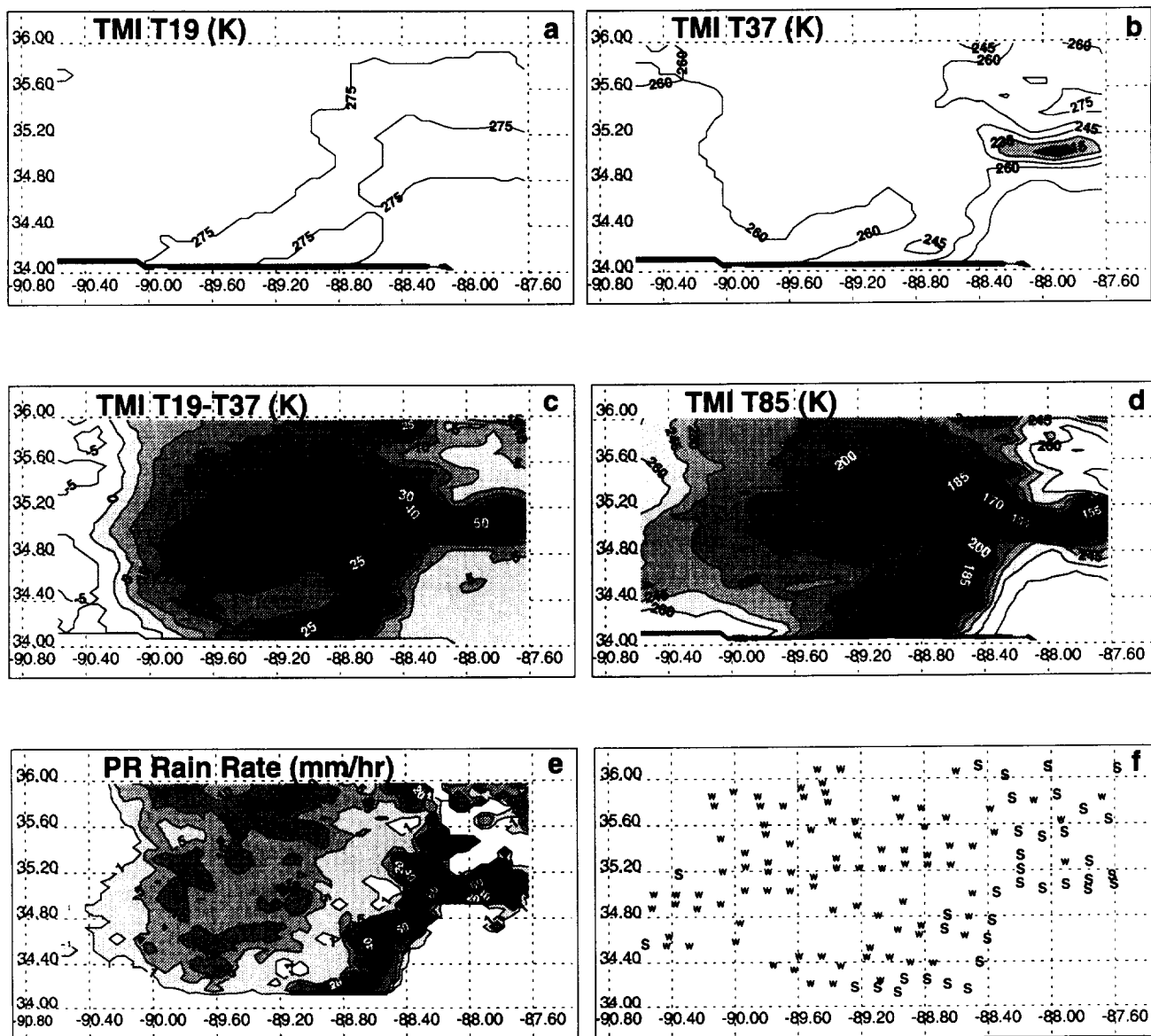


Figure 1: Maps of a) T19, b) T37, c) (T19-T37), d) T85, e) PR near-surface rain rate, and f) local minima in T85 for a mesoscale convective system observed by the TRMM satellite on 5 June 1998 over the Southeast United States. In Fig. 1f, local minima that are inferred to be strong and weak Cbs from the T85 spatial information are denoted with the letters S and w, respectively. Note that the brightness temperatures T19, T37, and T85 represent vertical polarization measurements.

correspond closely in space to maxima in rain rate, i.e., thunderstorms (Cbs), in the map of PR rain rate. Strong and weak Cbs deduced from the TMI data are denoted in Fig. 1f with the letters **S** and **w**, respectively. Outside of Cbs, the average rain rate is much weaker than that within Cbs.

From Figs. 1a and 1b, we observe that the 19 GHz and 37 GHz channels on land do not reveal rain information clearly. However, a map of the difference, (T19-T37), presented in Figure 1c compares well with the PR rain rate patterns (see Figure 1e), and it is similar to the map of T85 shown in Figure 1d. Such information given by the microwave radiometer and the radar is noticed over widely different tropical land regions.

We show in Figure 2a, a vertical cross section of the radar reflectivity taken from TRMM PR along a sub-satellite track. This cross section, which starts at (35.1° N, 90.6° W) and ends at (35.0° N, 87.6° W), corresponds to the same MCS depicted in Figs. 1a-f. The PR reflectivity below the 1 km level is not shown in this figure to avoid problems related to signal clutter arising from surface topography. We note from Fig. 2a that the leading edge of the storm, with its tall convective towers, is near 88° W. High reflectivity cores (> 30 dBZ) that extend well above the freezing level (~5.0 km) characterize these convective towers. To the west of these convective towers, from 88.6° W to 90.3° W, and above the freezing level, we notice an extensive anvil cloud with an almost horizontally uniform pattern of reflectivity. Below the freezing level, underneath the anvil cloud, there is a bright band that is about 0.5 km in thickness. In the convective towers, there is intense convective rain below the freezing level, while there is relatively light stratiform rain beneath the bright band (see Figure 2c). Notice there is a small region referred to as the Bounded Weak Echo Region (BWER) between 88.4° W and 88.5° W in the layer from 2 km to 6 km, which is at the origin of the anvil cloud. Such a BWER has been described in earlier studies with the help of observations made by ground-based radars (see Houze, 1993). This description of the

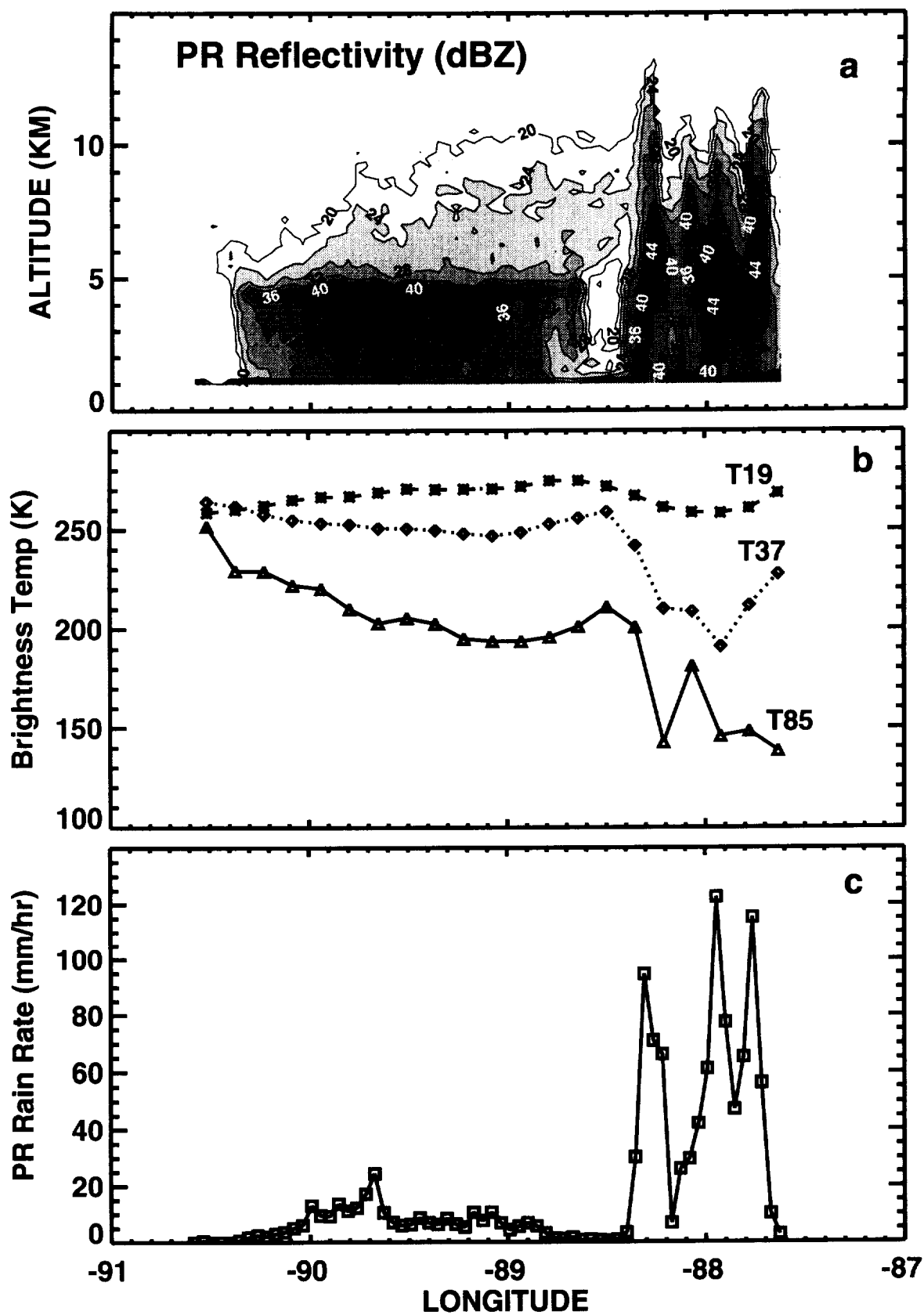


Figure 2: Vertical cross-sections of a) PR reflectivity, b) TMI T19, T37, and T85, and c) PR near-surface rain rate for the MCS presented in Figure 1 (see text for details).

reflectivity pattern and rain rate associated with a MCS is helpful in relating the TRMM PR observations with those of TMI.

In Figure 2b, the brightness temperatures measured by TMI in the 85, 37 and 19 GHz channels are shown along the sub-satellite track to correspond to the cross section of PR reflectivity shown in Fig. 2a. Note that TMI data shown in the figure are interpolated to the intersections of the conical-scans and the sub-satellite track. The PR data on the other hand are direct measurements along the sub-satellite track. In the response of the 85 GHz channel, we find there is a strong scattering depression due to relatively dense ice particles (Spencer et al., 1983) where the convective towers are present, but some of the individual towers shown in Fig. 2a are not well resolved in Fig. 2b. The anvil in the stratiform region produces weaker scattering depression. Over the entire cross-section domain, the response of the 37 GHz channel is similar to that of the 85 GHz channel, except that the scattering depression in 37 GHz is not as strong. The response in the 19 GHz channel is the weakest of the three channels. The interrelationship between TMI measured T85, T37, and T19, and the PR measured Z and R, is only crudely reflected in Figs. 2a-c, because of differences in the resolution of the TMI and PR data.

2.B. Convective and Stratiform Regions

One may notice from Figs. 1c-e, that the measurements made by TMI do not match closely in space with the near-surface rain rate deduced from PR. Although PR and TMI data are nearly simultaneous, such spatial mismatch is produced due to several reasons: a) the conical scanning geometry of TMI versus the cross-track scanning geometry of PR (Hong et al., 2000), b) differential advection and c) evolution of the hydrometeors in their transit from upper layers to lower layers in the atmosphere. This spatial mismatch is acute for the TMI 85 GHz channel because this channel responds to ice hydrometeors above the freezing level. For the 37 GHz channel this spatial mismatch is less severe, since it responds to lower layers of the atmosphere. In

this study, we are interested in comparing the information content of PR with that of TMI data in the 85, 37 and 19 GHz channels. For this purpose, we have assumed that averaging spatially the PR and TMI data minimizes spatial mismatch problems. In particular, we choose to average PR reflectivity at several altitudes and rain rate near the surface, and the TMI data in the 85 and 37 GHz channels, over the 19 GHz *fov* ($\sim 18 \times 30$ km²). All TMI and PR data averaged to the 19 GHz footprints are denoted from hereafter with an asterisk (*).

The PR data show that rain rate can be highly variable within a 19 GHz *fov*. In this *fov* there can be about 30 PR footprints of 4.3 km x 4.3 km size. These 30 footprints can be sorted according to the PR classification as having no rain, stratiform rain, or convective rain. In this study, a given 19 GHz *fov* that has a fractional area of convective rain that exceeds 50 % is categorized as convective. Similarly, a given 19 GHz *fov* that has a fractional area of stratiform rain that exceeds 80 % is categorized as stratiform. Of all the 19 GHz footprints in a MCS, only about 20 % meet these strict criteria of convective and stratiform nature. In order to obtain a sufficient sample of such convective and stratiform data for detailed analysis, we have utilized 20 MCS rain events observed by the TRMM satellite over diverse land regions of the tropics. To reduce contamination from wet land surfaces, the data where the polarization difference between the vertical and horizontal channels in the 19 GHz is greater than 5 K are eliminated.

Utilizing the data set described above, in Figure 3a we present a plot of T85* and the corresponding PR rain rate, R*. From this plot, we see that R* characterized as convective by the PR have relatively high rain rates and R* characterized as stratiform have generally low rain rates. There is a lot of scatter in the data, however, generally R* increases as T85* decreases.

To further enhance statistical strength of the data shown in Fig. 3a, we have performed additional averaging of the PR and TMI data. First, T85*, T37*, T19, R*, and Z* are sorted according to the T85* value. Then, in each 20 K interval of T85*, the values of T19, T37* and

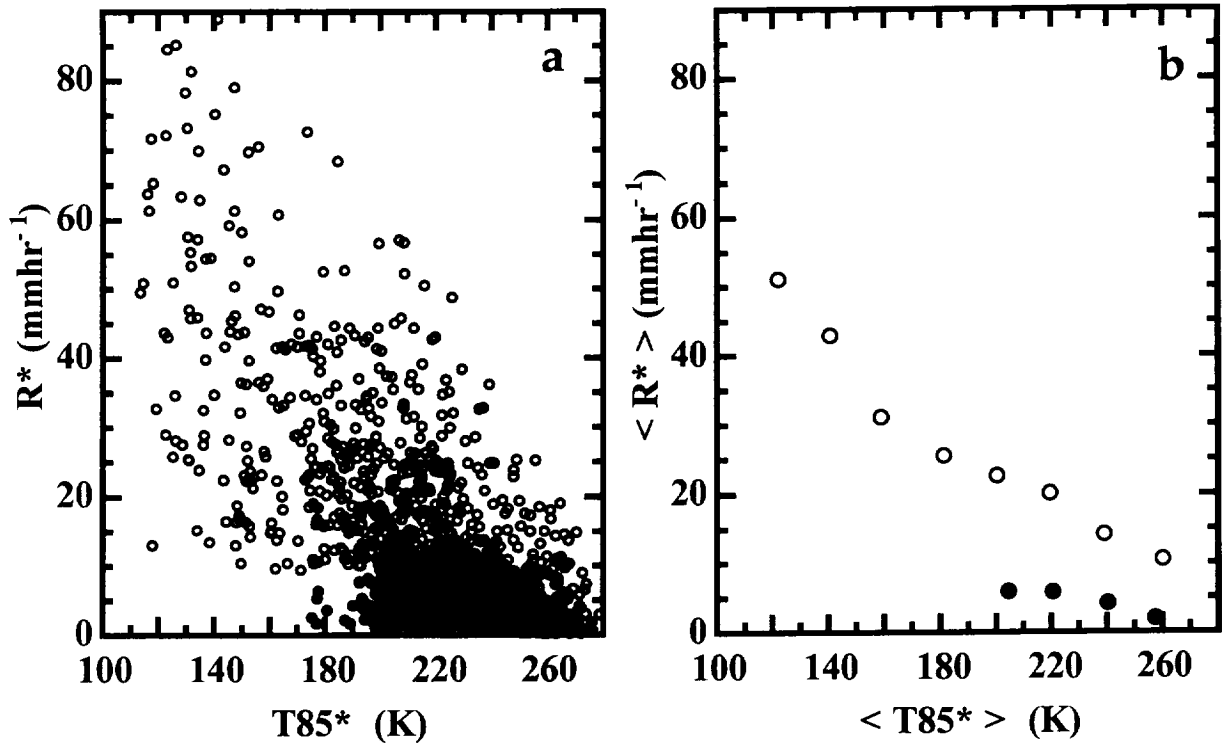


Figure 3: Scatter plots of a) R^* versus $T85^*$, and b) $\langle R^* \rangle$ versus $\langle T85^* \rangle$ based on PR and TMI observations of 20 MCS cases over diverse tropical land regions. The open circles in the plots denote observations from convective regions, while the filled circles represent observations from stratiform regions.

T85* are averaged to produce $\langle T19 \rangle$, $\langle T37^* \rangle$, and $\langle T85^* \rangle$. Similarly, the data from PR - i.e., R^* given by PR and the reflectivity, Z^* , at individual altitudes - are averaged to produce $\langle R^* \rangle$ and $\langle Z^* \rangle$. This has been done separately for convective and stratiform regions using the data from the 20 MCS events. In Tables 1a and 1b, $\langle T19 \rangle$, $\langle T37^* \rangle$, $\langle T85^* \rangle$, $\langle R^* \rangle$ and $\langle Z^* \rangle$ are presented. Each column in these tables represents a sequential 20 K interval in T85* and is identified alphabetically. The number of data that are averaged in each column is also shown in the tables. It may be pointed out that the standard deviation of all observations of Z^* at each altitude for a given T85* interval of 20 K has a magnitude that is comparable to the mean value itself. This suggests that there is a large diversity in the profiles for a small range in the brightness temperatures. Note, in the stratiform rain areas the magnitude of $\langle Z^* \rangle$ in the reflectivity profiles decreases below the melting layer. This decrease can be noticed all the way to the surface in Table 1b, and is apparently due to evaporation of rain drops below the freezing level. In each column of Tables 1a and 1b, we also present information pertaining to convective (C) and stratiform (S) rain fractions within a 19 GHz *fov*. Since these two rain fractions do not add up to 100 %, we can infer the rain-free area in each column. From Table 1a, we note on a scale of the 19 GHz *fov* the rain rate increases as the convective rain fraction increases.

Taking the averages given in Tables 1a and 1b, we present in Figure 3b the relationship between $\langle R^* \rangle$ and $\langle T85^* \rangle$ for the convective and stratiform regions. This figure shows that by substantially averaging the data, the noise in the Tbs produced by the three sources of spatial mismatch mentioned earlier is reduced, and a clear relationship between $\langle R^* \rangle$ and $\langle T85^* \rangle$ emerges. As indicated by theory, the convective rain rate increases non-linearly as $\langle T85^* \rangle$ decreases due to scattering by ice particles. The stratiform $\langle R^* \rangle$ increases slowly until $\langle T85^* \rangle$ decreases to about 220 K, due to scattering by ice aggregates.

Table 1: Average of PR and TMI data within a given 20 K interval of T85* for a) convective and b) stratiform rain. These averages are: $\langle T19 \rangle$, $\langle T37^* \rangle$, $\langle T85^* \rangle$, $\langle R^* \rangle$ and $\langle Z^* \rangle$. Also, convective and stratiform rain fractions are given. Note that $\langle Z^* \rangle$ is given for 1, 3, 4, 4.5, 6, 7, 9, and 11 km altitudes. The number of observations in a given T85 interval is also shown in these tables. The observations used to generate these statistics associated with convective and stratiform rain is deduced from 20 MCS cases over land regions.

a) Convective Rain Statistics

| | A | B | C | D | E | F | G | H |
|--------------------------------|---------|---------|---------|---------|---------|---------|---------|---------|
| T85 Interval (K) | 110-130 | 130-150 | 150-170 | 170-190 | 190-210 | 210-230 | 230-250 | 250-270 |
| # of Obs. | 21 | 48 | 48 | 102 | 139 | 132 | 78 | 51 |
| $\langle T85^* \rangle$ (K) | 121.9 | 140.4 | 159.0 | 181.2 | 200.2 | 219.5 | 239.1 | 259.9 |
| $\langle T37^* \rangle$ (K) | 200.1 | 215.5 | 229.5 | 244.4 | 252.5 | 258.7 | 265.3 | 271.2 |
| $\langle T19 \rangle$ (K) | 257.8 | 261.4 | 266.4 | 271.7 | 274.4 | 275.8 | 278.4 | 280.0 |
| C % | 91 | 87 | 83 | 77 | 72 | 73 | 65 | 64 |
| S % | 8 | 9 | 15 | 22 | 25 | 23 | 29 | 24 |
| $\langle R^* \rangle$ (mm/hr) | 51.2 | 43.0 | 31.2 | 25.6 | 22.7 | 20.2 | 14.2 | 10.6 |
| $\langle Z^* \rangle$ @ 1 km | 1.4E5 | 1.2E5 | 6.9E4 | 4.0E4 | 3.5E4 | 2.7E4 | 1.4E4 | 1.2E4 |
| $\langle Z^* \rangle$ @ 3 km | 1.4E5 | 1.1E5 | 6.7E4 | 3.1E4 | 2.3E4 | 1.8E4 | 1.1E4 | 8.0E3 |
| $\langle Z^* \rangle$ @ 4 km | 1.1E5 | 7.9E4 | 4.6E4 | 2.2E4 | 1.6E4 | 1.3E4 | 9.3E3 | 7.0E3 |
| $\langle Z^* \rangle$ @ 4.5 km | 8.3E4 | 6.0E4 | 3.3E4 | 1.5E4 | 1.1E4 | 9.4E3 | 7.2E3 | 5.6E3 |
| $\langle Z^* \rangle$ @ 6 km | 3.2E4 | 2.1E4 | 1.1E4 | 3.9E3 | 2.9E3 | 2.1E3 | 1.4E3 | 1.6E3 |
| $\langle Z^* \rangle$ @ 7 km | 1.6E4 | 1.0E4 | 5.9E3 | 1.9E3 | 1.4E3 | 7.9E2 | 5.0E2 | 6.6E2 |
| $\langle Z^* \rangle$ @ 9 km | 4.9E3 | 2.7E3 | 1.8E3 | 4.6E2 | 4.2E2 | 2.4E2 | 1.5E2 | 2.0E2 |
| $\langle Z^* \rangle$ @ 11 km | 1.5E3 | 8.2E2 | 7.2E2 | 2.1E2 | 1.9E2 | 9.6E1 | 7.3E1 | 3.5E1 |

b) Stratiform Rain Statistics

| | A | B | C | D |
|--|---------|---------|---------|---------|
| T85 Interval (K) | 190-210 | 210-230 | 230-250 | 250-270 |
| # of Obs. | 201 | 587 | 668 | 562 |
| $\langle T85^* \rangle$ (K) | 204.4 | 220.4 | 240.4 | 257.2 |
| $\langle T37^* \rangle$ (K) | 257.9 | 260.4 | 265.1 | 271.2 |
| $\langle T19 \rangle$ (K) | 275.9 | 277.2 | 279.3 | 280.7 |
| C % | 6 | 4 | 2 | 1 |
| S % | 94 | 96 | 97 | 95 |
| $\langle R^* \rangle$ ($\frac{\text{mm}}{\text{hr}}$) | 6.0 | 5.9 | 4.2 | 2.0 |
| $\langle Z^* \rangle @$ 1 km | 4.3E3 | 3.9E3 | 2.2E3 | 7.8E2 |
| $\langle Z^* \rangle @$ 3 km | 4.7E3 | 4.4E3 | 2.5E3 | 9.4E2 |
| $\langle Z^* \rangle @$ 4 km | 4.9E3 | 6.2E3 | 4.2E3 | 1.6E3 |
| $\langle Z^* \rangle @$ 4.5 km | 1.5E3 | 3.3E3 | 2.6E3 | 9.1E2 |
| $\langle Z^* \rangle @$ 6 km | 2.5E2 | 2.7E2 | 1.8E2 | 1.0E3 |
| $\langle Z^* \rangle @$ 7 km | 1.7E2 | 1.6E2 | 1.1E2 | 6.5E1 |
| $\langle Z^* \rangle @$ 9 km | 8.3E1 | 6.8E1 | 3.7E1 | 1.3E1 |
| $\langle Z^* \rangle @$ 11 km | 3.2E1 | 1.9E1 | 6.6E0 | 1.9E0 |

In Figures 4a and 4b, we present plots of $\langle Z^* \rangle$ at different altitudes in the atmosphere as a function of $\langle T85^* \rangle$ using the data given in Tables 1a and 1b. From Fig. 4a, we find that as $\langle T85^* \rangle$ increases from 120 K to 260 K, $\log_{10}\langle Z^* \rangle$ decreases systematically. In Fig. 4b, where the data for the stratiform rain are presented, we find that as $\langle T85^* \rangle$ increases from about 200 K to 260 K, $\log_{10}\langle Z^* \rangle$ also decreases systematically. The exception to this systematic decrease in the stratiform data is found when $\langle T85^* \rangle$ is near 200 K. This is likely due to evaporation below about 4.5 km.

In convective rain, despite the problems related to viewing geometry, the PR and TMI observations shown in Fig. 4a demonstrate that there is a relatively strong relationship between $\langle T85^* \rangle$ and the vertical profiles of $\langle Z^* \rangle$. The brightness temperatures $\langle T19 \rangle$ and $\langle T37^* \rangle$ have a weaker relationship with the radar reflectivity as shown in Table 1a. From this table, we note that the range in the values of $\langle T85^* \rangle$, $\langle T37^* \rangle$ and $\langle T19 \rangle$ from Column A to Column H are about 138 K, 71 K, and 23 K, respectively. The corresponding range in $\langle R^* \rangle$ is about 41 mmhr⁻¹. In the relatively pure stratiform regions, the ranges in $\langle T85^* \rangle$, $\langle T37^* \rangle$, and $\langle T19 \rangle$ are significantly reduced. In particular, the range of $\langle T85^* \rangle$ from Column A to D in Table 1b is only about 70 K. Furthermore, in the stratiform regions the rain rate, as well as its range, are only a few mmhr⁻¹.

Based on the data shown in Tables 1a and 1b, we note that for a given set of brightness temperatures - i.e., $\langle T19 \rangle$, $\langle T37^* \rangle$ and $\langle T85^* \rangle$ - one can get widely different rain rates depending on the type of rain that is being observed. As an example, one can compare the data shown in Column F of Table 1a and Column B of Table 1b. From these columns, we note when $\langle T85^* \rangle$ is close to 220 K, $\langle T37^* \rangle$ and $\langle T19 \rangle$ are close to 259 K and 276 K, respectively. However, we find near-surface rain rate, $\langle R^* \rangle$, deduced from PR for the convective rain is 20.2 mmhr⁻¹, while it is 5.9 mmhr⁻¹ for the stratiform rain. This implies that on average the multi-channel radiometer data has a poor ability to discriminate rain of different types, and thus can incur large errors in estimating rain

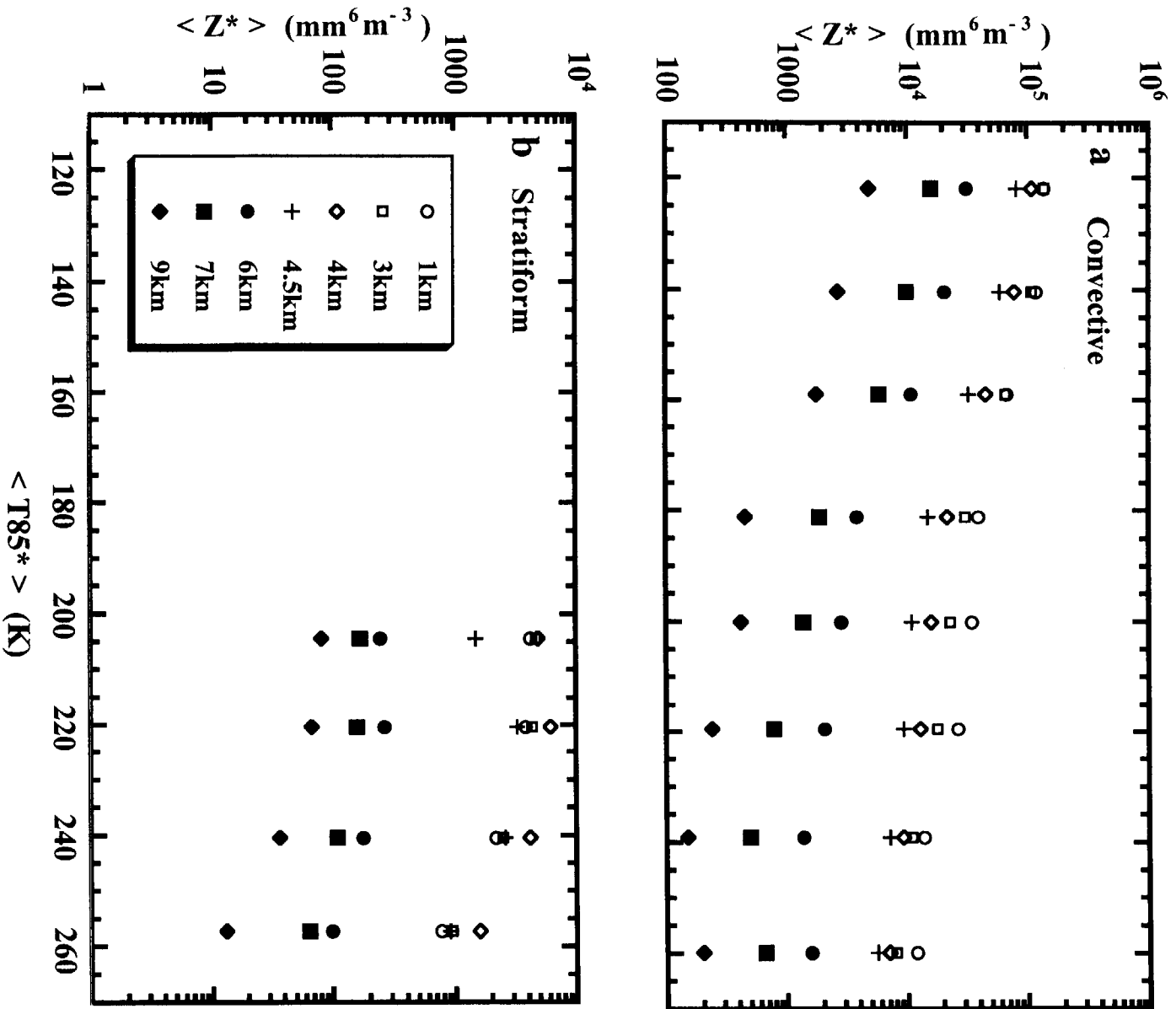


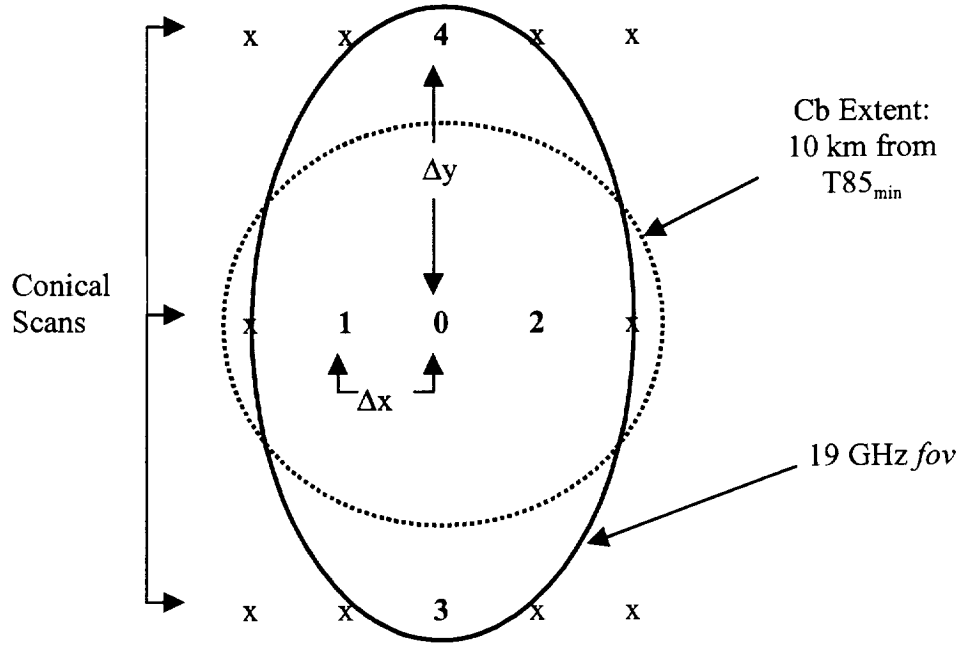
Figure 4: Average PR reflectivity, $\langle Z^* \rangle$, at different altitudes versus $\langle T85^* \rangle$ for a) convective and b) stratiform rain. The symbols denoting the various altitudes are shown as an inset in Panel b.

rate. Thus, specifying the nature of rain with information other than the magnitude of the brightness temperatures is necessary to estimate rain rate satisfactorily.

The observations of TMI and PR shown in Tables 1a and 1b can be simulated theoretically. In the study of Prabhakara et al. (2002), the average reflectivity profiles of PR presented in Tables 1a and 1b for convective and stratiform rain are utilized along with radiative transfer theory to calculate the brightness temperatures in the 85, 37 and 19 GHz channels of the TMI microwave radiometer. Details pertaining to the radiative transfer formalism, profiles of hydrometeors, and the results associated with these convective and stratiform simulations are presented in that study. These calculations lead us to infer that the link between the vertical profile of the reflectivity and the brightness temperatures measured by the radiometer, as shown in Tables 1a and 1b, can be simulated satisfactorily with theory. However, in these simulations, specification of a number of parameters is needed. These parameters pertain to the PSD, density, and phase - i.e., liquid, frozen, or mixed - of the hydrometeors in a vertical column of the atmosphere.

3. Discrimination of Cbs in MCSs Using TMI Data.

Since we cannot perfectly discriminate convective rain from stratiform rain using the microwave radiometer data, we have followed an alternate approach to retrieve rain from the TMI data. The TMI rain retrieval method developed in this study depends on our ability to discriminate strong and weak Cbs in the rain area. Based on the similarity between spatial patterns of rain rate, R , observed by PR and T_{85} measured by TMI, we have developed a method to discriminate these Cbs. We find that local minima in the T_{85} data, $T_{85_{\min}}$, relate closely in space to local maxima in rain rate given by PR (see Figs. 1e and 1f). In Figure 5, the scheme used to identify local minima in T_{85} is illustrated. These minima represent Cbs that typically have a scale of about 20 km. Two parameters from the TMI 85 GHz data are deduced to characterize the nature of rain in each Cb.



For TMI, $\Delta x = 4.6$ km, $\Delta y = 13.9$ km

Local Minima Definition
 When $T85_0 < T85_1$ and $T85_2$,
 Then $T85_{\min} = T85_0$

Approximation of Laplacian at Local Minima

$$\left. \frac{dT85}{dr} \right|_{5PT} = A(T85_1 + T85_2) + B(T85_3 + T85_4) - CT85_0$$

$$\left. \frac{dT85}{dr} \right|_{3PT} = 2A(T85_1 + T85_2 - 2T85_0)$$

$$A = 1/4\Delta x, \quad B = 1/4\Delta y, \quad C = (\Delta y / \Delta x + 1)/2\Delta y$$

$$\begin{aligned} \text{IF } \left. \frac{dT85}{dr} \right|_{5PT} > \left. \frac{dT85}{dr} \right|_{3PT} \quad \text{THEN } \frac{dT85}{dr} &= \left. \frac{dT85}{dr} \right|_{5PT} \\ \text{ELSE } \frac{dT85}{dr} &= \left. \frac{dT85}{dr} \right|_{3PT} \end{aligned}$$

Figure 5: TMI scan pattern showing the centers of 85 GHz footprints; the beam effective field of view of the 19 GHz (see also Kummerow et al., 1998); and a 10 km Cb that is collocated with a 19 GHz *fov*. Also illustrated is the method to determine the location of a T85 minimum, $T85_{\min}$, and the mean spatial gradient, $\left| dT85/dr \right|$, around this minimum.

The first is the magnitude of $T85_{\min}$, while the second is the Laplacian of T85, $\nabla^2 T85$, surrounding that minimum.

Ideally this Laplacian should be evaluated using the T85 value at the minimum and at four adjacent data points that are equally-spaced along orthogonal directions. However, we approximate this procedure, as depicted in Figure 5, with the data at the points 0 through 4. Three of these points, which include the minimum, are along one scan line, while the two others are on adjacent scan lines. The radially-averaged gradient of T85 using these five points, i.e., $\overline{dT85/dr}$, approximates the value of the Laplacian at the minimum. Here, r is the radial distance with respect to the minimum. However, when this five-point scheme is used to compute the Laplacian, its magnitude is often underestimated. This is due to the wide spacing (~ 14 km) between successive conical scan lines of the TMI radiometer (see Fig. 5). When this underestimation occurs, we assume that the Laplacian may be further approximated using only the data from three successive points along a scan line.

In order to distinguish weak Cbs from strong Cbs, we utilize the parameter $\overline{dT85/dr}$. From observations of TMI and PR, we find that when $\overline{dT85/dr}$ has a magnitude greater than 1 Kkm^{-1} at the location of a minimum in T85, generally there is a strong Cb at that point (PIWD, 2000). When this gradient is less than 1 Kkm^{-1} at the location of a minimum in T85, that Cb is generally a weak one. As an example, a map of the Cbs identified in this manner is shown in Fig. 1f. Once a Cb has been determined to be strong or weak, T85 and (T19-T37) close to the center of the Cb can be used to determine average rain intensity in the Cb. In this study, each Cb is assumed to have a radius of 10 km from the Cb center. A Cb of this scale can influence five footprints along a conical scan line: the central local minimum, and the two adjacent 85 GHz footprints on either side (see Fig. 5). Any remaining 85 GHz footprints lie completely outside the influence of Cbs.

In order to demonstrate the usefulness of the above Cb discrimination method, we have isolated $\overline{T85^*}$, $\overline{T37^*}$, $\overline{T19}$, and $\overline{R^*}$ belonging to three rain categories: strong Cbs, weak Cbs, and regions outside of Cbs. These data are taken from the 20 MCS rain events referred to in Section 2. In Table 2, in each category averages of $\overline{R^*}$, $\overline{T85^*}$, and $(\overline{T19 - T37^*})$ have been computed. These averages are respectively denoted as $\overline{R^*}$, $\overline{T85^*}$, and $\overline{T19 - T37^*}$. We also show in Table 2, the population of the data for the above three rain categories. The information associated with the three rain categories, along with corresponding percentages of convective and stratiform rain given by the PR, are presented in this table.

Table 2: For 1) Strong Cbs ($\overline{dT85/dr} > 1 \text{ Kkm}^{-1}$), 2) Weak Cbs ($0 < \overline{dT85/dr} \leq 1 \text{ Kkm}^{-1}$), and 3) Areas Outside of Cbs inferred from TMI data: PR observed convective and stratiform rain fractions and rain rates, $\overline{R^*}$; and TMI observed $\overline{T85^*}$ and $\overline{T19 - T37^*}$.

| Cb Category | Data Count | Conv Rain Fraction (%) | Strat Rain Fraction (%) | $\overline{R^*}$ (mmhr ⁻¹) | $\overline{T85^*}$ (K) | $\overline{T19 - T37^*}$ (K) |
|-------------|------------|------------------------|-------------------------|--|------------------------|------------------------------|
| Strong | 296 | 42 | 48 | 12.6 | 212.0 | 12.6 |
| Weak | 522 | 11 | 83 | 5.5 | 225.3 | 5.5 |
| Outside | 2655 | 3 | 31 | 0.8 | 262.7 | 0.8 |

From Table 2, we note that the convective rain fraction and rain rate decrease substantially from the strong Cbs to the weak Cbs, while the stratiform rain fraction behaves in an opposite manner. It is $\overline{dT85/dr}$ used in our method that is responsible for crudely identifying these categories. The number of data outside of the Cbs is large, and several of them are close to the edge of the rain area. Due to partial footprint coverage, this leads to relatively small $\overline{R^*}$ and warm $\overline{T85^*}$ in this category. Partitioning the TMI data using the method described above helps considerably in the formulation of the rain retrieval method developed here.

4. TMI Rain Retrieval Method

In Section 2.A, we showed that the information about PR rain rate in Fig. 1e is best revealed by the TMI observed (T19-T37) and T85 presented in Figs. 1c and 1d, respectively. In order to appreciate the rain information conveyed by T85 and (T19-T37), we show in Figure 6 average PR rain rate as a function of these two TMI variables. From this figure, we note that generally rain rate increases as (T19-T37) increases, while it increases as T85 decreases. This behavior tends to be non linear. In addition, a Cb component of rain is imbedded in the average rain rate shown in Fig. 6. This contributes to large variability in the rain information shown in this figure. In this study, as pointed out earlier, the convective rain from Cbs is inferred with the help of the variable $\overline{dT85/dr}$, calculated at local minima in T85. From this discussion, we choose to express the relationship between R and the TMI measurements as follows:

$$R = f \left[(T19 - T37), T85, \left. \frac{dT85}{dr} \right|_{T85 \min} \right] . \quad (1)$$

However, in this equation $\overline{dT85/dr}$ serves only as a gross parameter to represent the variables that are necessary to retrieve rain rate, i.e. PSD, density, and phase - liquid, frozen, or mixed - of the hydrometeors in a vertical column of the atmosphere. So, for the purpose of retrieving rain rate from the radiometer data, it is preferable to simplify this non linear function given in Eq. 1 empirically with the help of TMI and PR observations.

In the current TMI-V5 Algorithm, a statistical regression equation developed by Grody et al. (1991) is incorporated into the Bayesian procedure to make rain rate estimates over land from the TMI data. There is scope to improve this method, because this regression formalism does not satisfactorily discriminate convective and stratiform rain types (Kummerow, 2001). In the present

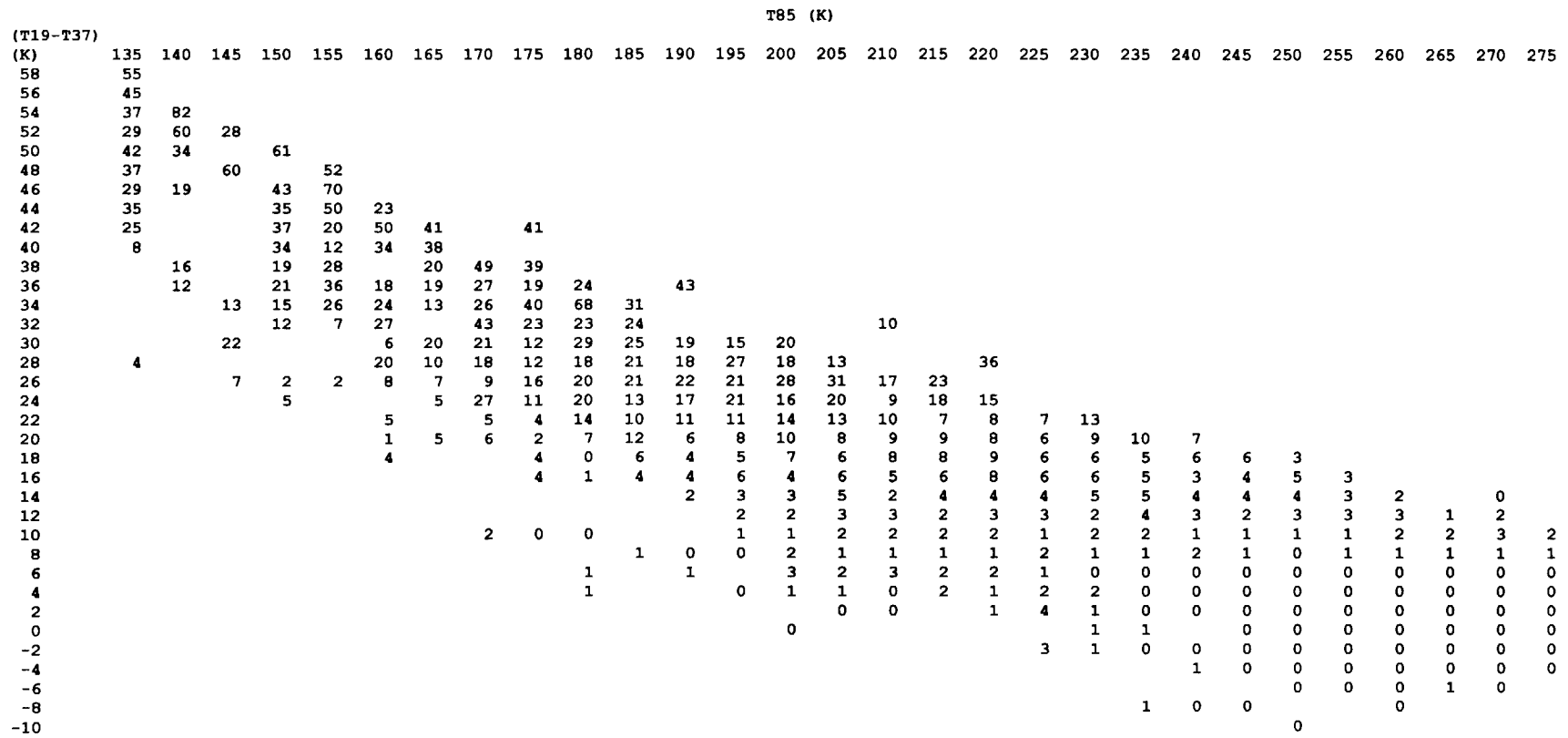


Figure 6: Plot of PR rain rate (mmhr^{-1}) averaged in discrete bins of 2 K for (T19-T37) and 5 K for T85, utilizing the TMI and PR data from 20 MCS cases over diverse tropical land regions.

study, we have created a rain retrieval model that crudely differentiates rain types, as shown in Table 2.

In our rain retrieval algorithm, referred to hereafter as the TMI-Cb Algorithm, we screen out the data using the polarization difference in the 19 GHz channel. Then, we assume there is a very weak (background) rain rate, R_B , at every 85 GHz footprint where T85 is less than 270 K. Since there is no rigorous theoretical basis to assign zero rain rate to a particular brightness temperature, based on the TRMM observations, we assume that rain rate is 0.0 mmhr^{-1} when T85 is equal to or greater than 270 K. Also, we infer from the radar observations (Fig. 3b) that when T85 is less than 200 K the rain is dominantly of convective type, while when T85 is greater than 200 K there is a mix of convective and stratiform rain. For this reason, in our rain retrieval method we assume the non-linear relationship between the background rain rate, R_B , and T85 may be approximated with two linear segments. These segment have different slopes and a break point at T85 equal to 200 K. These relationships for background rain rates are expressed with appropriate constants B_1 and B_2 as follows:

$$\begin{cases} R_B = B_1 (270 - T85) & \text{when } 270 > T85 > 200\text{K} \\ R_B = 70B_1 + B_2 (200 - T85) & \text{when } T85 \leq 200\text{K} \end{cases} \quad (2)$$

The constants B_1 and B_2 have values of 0.075 and $0.15 \text{ mmhr}^{-1}\text{K}^{-1}$, respectively. On the basis of Eq. 2, the areas outside of Cbs, where T85 is typically greater than 200 K, will have a very weak rain rate ($< 5 \text{ mmhr}^{-1}$). On the other hand, when T85 is significantly less than 200 K, which typically occurs within Cbs, the background rain rate inferred from Eq. 2 can be higher than 5 mmhr^{-1} . We relate R_B to T85 because it responds strongly to ice aggregates in stratiform rain regions, and as a result is better suited to estimate very weak rain rates.

In the TMI-Cb Algorithm, each strong and weak Cb is assumed to have a 10 km radius from the center of the T85 minimum. Within these Cbs, we assume the background rain rate, R_B , is enhanced with a Cb component of rain rate, R_r . Thus, an estimate of the total rain rate at any 85 GHz footprint is given by the sum of R_B and R_r . To retrieve R_r , information pertaining to (T19-T37), T85, and $\overline{dT85/dr}$ at the T85 minimum is utilized. For this purpose, we have adopted a simple equation, which has the following form:

$$R_r = \alpha[(T19 - T37) - \beta(T85' - T85_{\min})] . \quad (3)$$

In this equation, α and β are constants, and T85' is a reference value of 85 GHz brightness temperature. Separate relationships of the above form are developed for strong Cbs ($\overline{dT85/dr} > 1$ Kkm⁻¹) and weak Cbs ($0 < \overline{dT85/dr} \leq 1$ Kkm⁻¹).

Analogous to Equation 2, we relate rain rate in the weak Cbs, R_{rw} , to TMI observations with two equations. As remarked earlier, the T85 value of 200 K delineates crudely a transition in the nature of rain. For this reason, to determine R_{rw} one equation is used when $T85_{\min}$ is less than 200 K, and another equation is used when $T85_{\min}$ is greater than 200 K. These equations are given as follows:

$$\text{Weak Cbs} \quad \begin{cases} R_w = W_1[(T19 - T37) - D(270 - T85_{\min})] & \text{when } 270K > T85_{\min} > 200K \\ R_w = W_2[(T19 - T37) - D(270 - T85_{\min})] & \text{when } T85_{\min} \leq 200K \end{cases} . \quad (4)$$

Similarly, to determine the rain rate in strong Cbs, R_{rs} , two such equations are adopted as follows:

$$\text{Strong Cbs} \begin{cases} R_s = S_1 [(T19 - T37) - D(270 - T85_{\min})] & \text{when } 270K > T85_{\min} > 200K \\ R_s = S_2 [(T19 - T37) - D(270 - T85_{\min})] & \text{when } T85_{\min} \leq 200K \end{cases} \quad (5)$$

Note, the constants in Eqs. 2, 4 and 5 - i.e., B_1 , B_2 , W_1 , W_2 , S_1 , S_2 , and D - are calibrated using the PR observations taken from a limited number of MCS cases (20) in diverse land regions over the tropics. Given the value of these constants (see Table 3), the scheme is applied to the TMI data to retrieve rain over several $5^\circ \times 5^\circ$ land regions for a period of three months.

Table 3: Values of the constants used in Eqs. 2, 4, and 5.

| | | | | | | |
|-------|-------|-------|-------|-------|-------|-------|
| D | B_1 | B_2 | W_1 | W_2 | S_1 | S_2 |
| 0.133 | 0.075 | 0.15 | 0.25 | 0.7 | 0.5 | 0.7 |

5. Results

We have estimated rain rates over $5^\circ \times 5^\circ$ (lat. x long.) areas for 5 different land regions in the tropics. These retrievals are performed for each overpass of the TRMM satellite within each land area for a three month period. The details of these regions and the time periods are presented in Table 4.

Table 4: List of $5^\circ \times 5^\circ$ land regions and the time periods used in our analysis.

| Region | Lat Bounds | Long Bounds | Number of Overpasses | Season |
|-----------|---------------|---------------|----------------------|------------|
| Amazon | -8.5 : -3.5 | -68.5 : -63.5 | 124 | DJF:2000-1 |
| Australia | -18.8 : -13.8 | 130.3 : 135.3 | 132 | DJF:2000-1 |
| India | 20.0 : 25.0 | 79.0 : 84.0 | 150 | JJA:2000 |
| Nigeria | 5.5 : 10.5 | 7.5 : 12.5 | 127 | JJA:2000 |
| SE Asia | 17.5 : 22.5 | 99.5 : 104.5 | 144 | JJA:2000 |

From each overpass of the TRMM satellite in a given $5^\circ \times 5^\circ$ region, we have calculated area-average rain rate, R^A , defined as follows:

$$R^A = \frac{\sum_{n=1}^N R_n^*}{N} \quad (6)$$

In this equation, N represents the total number of data covering the portion of the 220 km PR swath in the $5^\circ \times 5^\circ$ region. The area-average rain rate for the PR, TMI-Cb Algorithm, and TMI-V5 Algorithm are denoted as R_{PR}^A , R_{Cb}^A , and R_{V5}^A . In Table 5a, we show that the correlation coefficient between R_{PR}^A and R_{Cb}^A (~ 0.87) is higher over all tropical land regions when compared to the correlation given by R_{PR}^A and R_{V5}^A (~ 0.83). To illustrate this result, in Figure 7 R_{PR}^A is compared against R_{Cb}^A and R_{V5}^A for the Amazon $5^\circ \times 5^\circ$ region.

Table 5: Correlation between PR rain rate and rain rates retrieved from the TMI-Cb and TMI-V5 Algorithms. **a)** Correlation on the large scale ($\leq 220 \times 550 \text{ km}^2$). **b)** Correlation on the scale of the 19 GHz *fov* ($\sim 18 \times 30 \text{ km}^2$).

a) Large Scale

| $5^\circ \times 5^\circ$ Region | R_{Cb}^A vs. R_{PR}^A | R_{V5}^A vs. R_{PR}^A |
|---------------------------------|---------------------------|---------------------------|
| Amazon | 0.78 | 0.7 |
| Australia | 0.89 | 0.88 |
| India | 0.92 | 0.87 |
| Nigeria | 0.95 | 0.94 |
| S. E. Asia | 0.8 | 0.75 |
| Mean | 0.87 | 0.83 |

b) Scale of 19 GHz *fov*

| $5^\circ \times 5^\circ$ Region | R_{Cb}^* vs. R_{PR}^* | R_{V5}^* vs. R_{PR}^* |
|---------------------------------|---------------------------|---------------------------|
| Amazon | 0.64 | 0.54 |
| Australia | 0.6 | 0.5 |
| India | 0.64 | 0.56 |
| Nigeria | 0.64 | 0.56 |
| S. E. Asia | 0.69 | 0.64 |
| Mean | 0.64 | 0.56 |

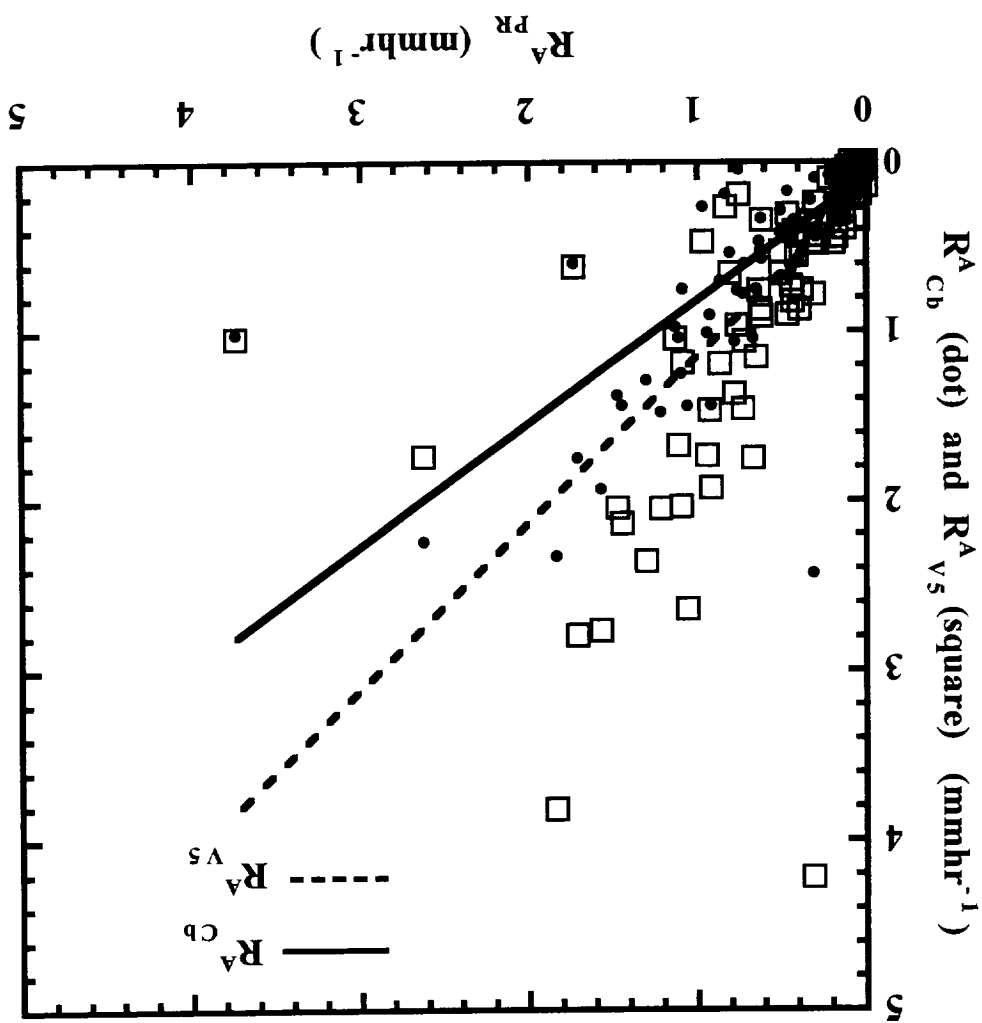


Figure 7: Scatter plot of large-scale, area-averaged rain rates R^A_{PR} versus R^A_{Cb} and R^A_{Vs} for the Amazon $5^\circ \times 5^\circ$ region (see text for details). The correlation between R^A_{PR} and R^A_{Cb} is 0.78, while it is 0.70 between R^A_{PR} and R^A_{Vs} .

The correlation between the area-average rain rates over the large-scale presented in Table 5 gives only a crude comparison, since such averages are insensitive to the fine spatial details in the rain pattern. For this reason, we have performed a statistical evaluation of the rain rates given by the PR, TMI-Cb Algorithm, and TMI-V5 Algorithm averaged on the scale of the 19 GHz *fov* (see Section 2.B). These rain rates are respectively represented as R^*_{PR} , R^*_{Cb} and R^*_{V5} . Such an evaluation is particularly valuable, because it can reveal the weakness in a radiometer retrieval algorithm. In particular, the radiometer techniques have a weakness to discriminate convective and stratiform rain that is clearly revealed by the radar (Kummerow et al., 2001). In Table 5b, we show that the correlation coefficient between R^*_{PR} and R^*_{Cb} (~ 0.64) is much higher over all tropical land regions when compared to the correlation given by R^*_{PR} and R^*_{V5} (~ 0.56). As an example, we present in Figure 8a a scatter plot of R^*_{PR} versus R^*_{Cb} for the Amazon $5^\circ \times 5^\circ$ region. A similar scatter plot of R^*_{PR} versus R^*_{V5} is presented in Figure 8b. From Fig. 8b, we may note that the bulk of the rain rates between 0 and 10 mmhr⁻¹ are overestimated in the TMI-V5 Algorithm compared to the PR. This is not the case with TMI-Cb rain rates, as shown in Fig. 8a.

We may point out that the two TMI derived rain rates averaged on the 19 GHz *fov* correlate poorly with the PR rain rate. There are three main reasons for this poor correlation. These reasons are 1) spatial mismatch between TMI and PR information (discussed in Section 2.B), 2) TMI brightness temperatures differentiate poorly convective and stratiform rain (see Tables 1a and 1b), and 3) evaporation and imbedded rain-free areas are not reflected in the TMI data.

In Figures 9a-c, we show maps of the spatial patterns of rain rate for a rain event that occurred over the Amazon on 8 August 2000 based on the PR, TMI-Cb Algorithm, and TMI-V5 Algorithm, respectively. Compared to the PR and TMI-Cb Algorithm, the TMI-V5 Algorithm shows rain rates greater than 10 mmhr⁻¹ over a large region.

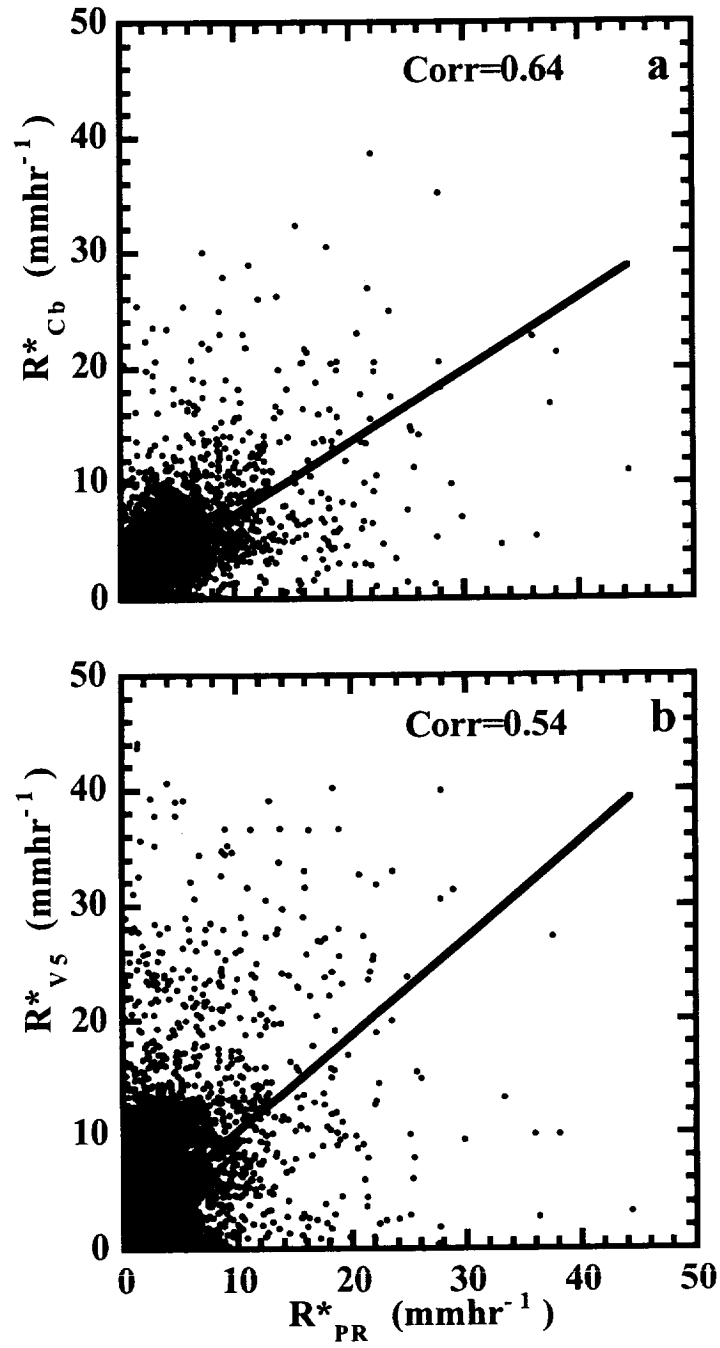


Figure 8: Scatter plots of a) R^*_{PR} versus R^*_{Cb} , and b) R^*_{PR} versus R^*_{VS} for the Amazon $5^\circ \times 5^\circ$ region. Note, R^*_{PR} , R^*_{Cb} , and R^*_{VS} represent averages over 19 GHz footprints.

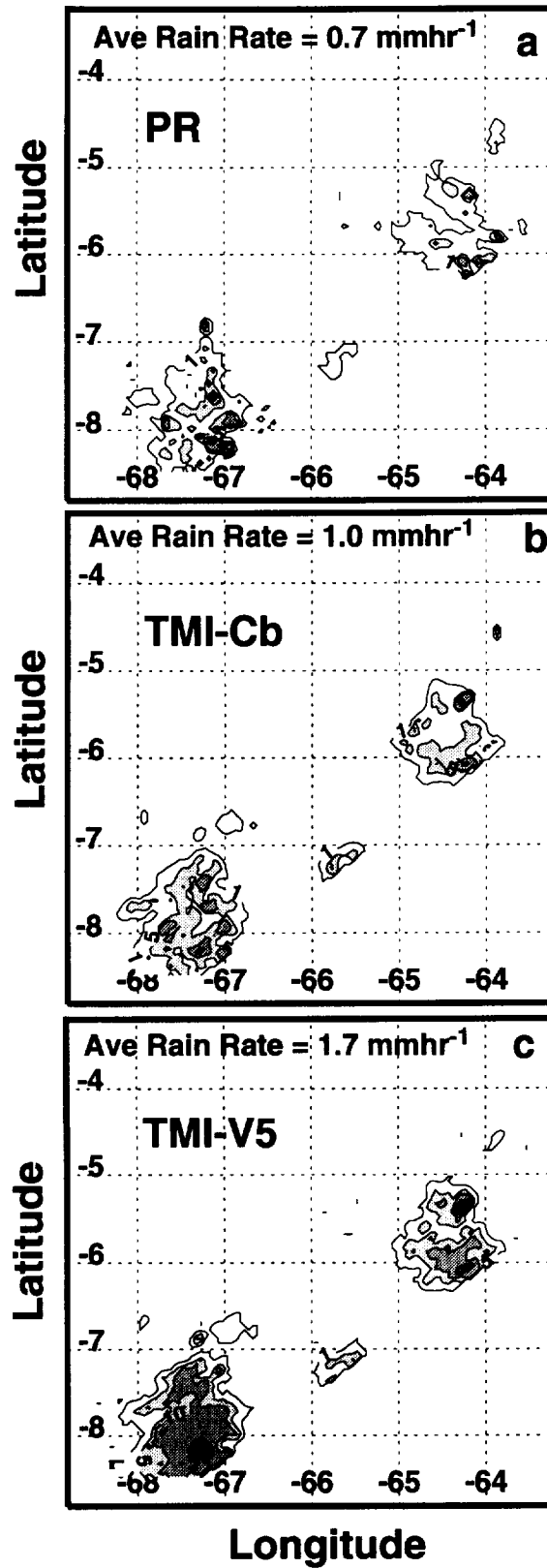


Figure 9: Rain patterns given by the a) PR, b) TMI-Cb Algorithm, and c) TMI-V5 Algorithm for a TRMM satellite overpass of the Amazon region that occurred on 8 December 2000 (orbit number 17446).

The improvement in rain retrieval from our TMI-Cb Algorithm results from a) separation of different rain types with the help of Cbs, and b) use of separate relationships between rain rates and Tbs for each rain type. This algorithm can be applied to the full 760 km swath of the TMI, which is well beyond the narrow 220 km swath of the PR observations. As a result, one can obtain better estimates of latent heat release into the atmosphere (Iacovazzi, 2001) over a wider area, which in turn can be used to improve general circulation models.

6. Conclusions

Multi-spectral, dual-polarization measurements made by satellite-borne microwave radiometers do not contain enough independent pieces of information to derive the amount and the vertical distribution of liquid, mixed-phase, and frozen hydrometeors present in the atmosphere (see Schols et al., 1999). This leads to uncertainties in quantitative estimation of rain rate deduced from microwave radiometers pertaining to convective and stratiform rain based purely on radiative transfer theoretical considerations. In addition, the retrieval of rain from microwave radiometers is further complicated over land. This is because the spectral signal pertaining to rain in the long wavelength channels (19 and 37 GHz) is weak over land regions, because of reduced brightness temperature contrast between the surface and the clouds. Additional information, that is independent of the spectral measurements, is therefore necessary over land to derive rain quantitatively.

In the TMI-V5 Algorithm, a multiple regression method, based on brightness temperature data, is utilized to retrieve rain rate on land from TMI. Since different rain types are not well resolved in this approach, the contrast in rain rate between them is not represented adequately. On the other hand, in the TMI-Cb Algorithm developed in this study, special attention is given to separating the TMI data crudely into different rain types. For this purpose, minima in the spatial distribution of T85 are used to identify Cbs. These Cbs have enhanced convective rain, compared

to the much lighter rain rates present in the areas outside of Cbs. In addition, the average gradient of T85 immediately around each minimum is used to distinguish two different types of Cbs, strong and weak. With the help of this discrimination procedure, we are able to deduce a relationship between the brightness temperatures and rain rate for the two types of Cbs, and areas outside of Cbs.

Spatial information, derived from satellite infrared radiometer observations, has been utilized empirically in an earlier study by Adler and Negri (1988) for the purpose of obtaining convective and stratiform rain. However, since microwave data represent properties of the dense layers in precipitating clouds, and not just a thin layer near the cloud tops, microwave techniques perform better than infrared techniques in retrieving instantaneous estimates of rain rate (Ebert et al., 1996).

When this TMI-Cb Algorithm is applied to a large volume of TMI data collected over several 5°x5° tropical land areas for a period of three months, we find that this algorithm can give improved rain retrievals compared to the TMI-V5 Algorithm. This analysis suggests that the current TMI-V5 Algorithm applied to the land could be improved by adopting the methodology shown in this study.

As indicated in this study, the information about rain given by the low frequency channels - i.e., T19-T37 - can yield better information about convective rain compared to the 85 GHz. For this reason, to improve the state-of-the-art of rain retrieval, we contend that a radiometer having 19 and 37 GHz channels with the same *fov* is preferable to minimize surface contamination. Also, it is preferable to have a radiometer that has a finer resolution (~ 5 - 10 km) for both of these channels.

An important consideration in the TMI-Cb Algorithm is the identification of minima in T85. Liu and Curry (1998, 1999, and 2000) have demonstrated the usefulness of the 150 GHz channel to infer ice water content in the upper layers of the troposphere. Because of its higher frequency, for

the same size of antenna, a channel near 150 GHz can yield a spatial resolution that is about two times better than the 85 GHz. We find that this high extinction and spatial resolution could be extremely valuable in isolating brightness temperature minima corresponding to convective cells in vigorously developing and decaying thunderstorms. Also, 150 GHz radiation is more opaque to water vapor than that at 85 GHz. This makes a 150 GHz channel useful in the middle and high latitudes, where surface contamination becomes a problem at 85 GHz. From these considerations, we contend that microwave radiometers with a conical-scanning geometry that yields spatially continuous observations in a 150 GHz channel will be valuable for the remote sensing of rain.

Understanding the relationship between the measurements made by microwave radiometers and convective and stratiform rain is necessary for the future Global Precipitation Measurement (GPM) mission (E. A. Smith, personal communication). In GPM, a constellation of satellites with microwave radiometers are expected to be flown without an accompanying radar. This will also be the case with microwave radiometers onboard the Earth Observing System's Aqua satellite and the Japanese satellite ADEOS-II. Thus, the present study has useful applications for future satellite missions.

Acknowledgments

During this research, Dr. Yoo was supported by the Climate Environment System Research Center sponsored by the SRC program of Korea Science Engineering Foundation. Also, the TRMM data for this research was supplied by the Distributed Active Archive Center (DAAC) of NASA Goddard Space Flight Center.

References

- Adler, R. F. and A. J. Negri, 1988: A satellite infrared technique to estimate tropical convection and stratiform rainfall. *J. Appl. Met.*, **27**, 30-51.
- Balakrishnan, N. and D. S. Zmic, 1990: Estimation of rain and hail rates in mixed-phase precipitation. *J. Atmos. Sci.*, **47**, 565-583.
- Bringi, V. N., K. Knupp, A. Detwiler, L. Lui, I. J. Caylor, and R. A. Black, 1997: Evolution of a Florida thunderstorm during the Convective and Precipitation/ Electrification Experiment: The case of 9 August 1991. *Mon. Wea. Rev.*, **125**, 2131-2160.
- Conner, M. D., and G. W. Petty, 1998: Validation and intercomparison of SSM/I rain-rate retrieval methods over the continental United States. *J. Appl. Met.*, **37**, 679-700.
- Ebert, E. E., M. J. Manton, P. A. Arkin, R. J. Allam, G. E. Holpin, and A. Gruber, 1996: Results from the GPCP Algorithm Intercomparison Programme. *Bull. of Am. Met Soc.*, **77**, 2875-2887.
- Grody, N. C., 1991: Classification of snow cover and precipitation using Special Sensor Microwave Imager. *J. Geophys. Res.*, **96**, 7423-7435.
- Hong, Y., C. D. Kummerow, and W. S. Olson, 1999: Separation of convective and stratiform precipitation using microwave brightness temperature. *J. Appl. Met.*, **38**, 1193-1213.
- Hong, Y., J. L. Haferman, W. S. Olson, and C. D. Kummerow, 2000: Microwave brightness temperatures from tilted convective systems. *J. Appl. Meteor.*, **39**, 983-998.
- Houze Jr., R. A., 1993: *Cloud Dynamics*. Academic Press, Inc., San Diego, 571 pp.
- Houze Jr., R. A., 1997: Stratiform precipitation in regions of convection: A meteorological paradox? *Bull. Amer. Met. Soc.*, **78**, 2179-2196.
- Iacovazzi, Jr., R. A., 2001: A simple one-dimensional model to estimate mesoscale atmospheric latent heating profiles from TRMM rain statistics. Ph.D. dissertation, University at Albany, State University of New York, Albany, NY, 92 pp.
- Iguchi, T., T. Kozu, R. Meneghini, J. Awaka, and K. Okamoto, 2000: Rain-profiling algorithm for the TRMM Precipitation Radar. *J. Appl. Met.*, **39**, 2038-2052.

- Kummerow, C., R. A. Mack, and I. M. Hakkarinen, 1989: A self-consistency approach to improved microwave rainfall estimation from space. *J. Appl. Met.*, **28**, 869-884.
- Kummerow, C., W. S. Olson, and L. Giglio, 1996: A simplified scheme for obtaining precipitation and vertical hydrometeor profiles from passive microwave sensors. *IEEE Trans. Geosci. Remote Sens.*, **34**, 1213-1232.
- Kummerow, C., W. Barnes, T. Kozu, J. Shiue, and J. Simpson, 1998: The Tropical Rainfall Measuring Mission (TRMM) sensor package. *J. Atmos. Oceanic Tech.*, **15**, 808-816.
- Kummerow, C. and Coauthors, 2001: The evolution of the Goddard Profiling Algorithm (GPROF) for rainfall estimation from passive microwave sensors. *J. Appl. Met.*, **40**, 1801-1820.
- Liu, G. and J. A. Curry, 1998: Remote sensing of ice water characteristics in tropical clouds using aircraft microwave measurements. *J. Appl. Met.*, **37**, 337-355.
- Liu, G. and J. A. Curry, 1999: Tropical ice water amount and its relations to other atmospheric hydrological parameters as inferred from satellite data. *J. Appl. Met.*, **38**, 1182-1194.
- Liu, G. and J. A. Curry, 2000: Determination of ice water path and mass median particle size using multi-channel microwave measurements. *J. Appl. Met.*, **39**, 1318-1329.
- Olson, W. S., C. Kummerow, Y. Hong, and W.-K. Tao, 1999: Atmospheric latent heating distributions in the tropics derived from satellite passive microwave radiometer measurements. *J. Appl. Met.*, **38**, 633-664.
- Prabhakara C., R. Iacovazzi, Jr., J. A. Weinman, and G. Dalu, 2000: A TRMM microwave radiometer rain rate estimation method with convective and stratiform discrimination. *J. Met. Soc. Japan*, **78**, 241-258.
- Prabhakara, C., R. Iacovazzi, Jr., and J.-M. Yoo, 2002: Simulation of TRMM Microwave Imager brightness temperature using Precipitation Radar reflectivity for convective and stratiform rain areas over land. NASA Tech. Memo. #2002-210000, 56 pp.
- Sax, R. I. and V. W. Keller, 1980: Water-ice and water-updraft relationships near -10°C with populations of Florida cumuli. *J. Appl. Met.*, **19**, 505-514.

- Schols, J. L., J. A. Weinman, G.D. Alexander, R. E. Stewart, L.J. Angus, and A.C.L. Lee, 1999: Microwave properties of frozen precipitation around a North Atlantic cyclone. *J. Appl. Met.*, **38**, 29-43.
- Simpson, J., C. Kummerow, W.-K. Tao, and R. F. Adler, 1996: On the tropical rainfall measuring mission (TRMM). *Met and Atmos. Phys.*, **60**, 19-36.
- Smith, P. L., D. J. Musil, A. G. Detwiler, and R. Ramachandran, 1999: Observations of mixed-phase precipitation within a CaPE thunderstorm. *J. Appl. Met.*, **38**, 145-155.
- Spencer, R. W., W. S. Olson, R. Wu, D. W. Martin, J. A. Weinman, and D. A. Santak, 1983: Heavy thunderstorms observed over land by the Nimbus 7 Scanning Multichannel Microwave Radiometer. *J. Climate and Appl. Meteor.*, **22**, 1041-1046.
- Wu, R. and J. A. Weinman, 1984: Microwave radiances from precipitating clouds containing aspherical ice, combined phase, and liquid hydrometeors. *J. Geophy. Res.*, **89**, 7170-7178.

Figure Captions

Figure 1: Maps of **a)** T19, **b)** T37, **c)** (T19-T37), **d)** T85, **e)** PR near-surface rain rate, and **f)** local minima in T85 for a mesoscale convective system observed by the TRMM satellite on 5 June 1998 over the Southeast United States. In Fig. 1f, local minima that are inferred to be strong and weak Cbs from the T85 spatial information are denoted with the letters **S** and **w**, respectively. Note that the brightness temperatures T19, T37, and T85 represent vertical polarization measurements.

Figure 2: Vertical cross-sections of **a)** PR reflectivity, **b)** TMI T19, T37, and T85, and **c)** PR near-surface rain rate for the MCS presented in Figure 1 (see text for details).

Figure 3: Scatter plots of **a)** R^* versus $T85^*$, and **b)** $\langle R^* \rangle$ versus $\langle T85^* \rangle$ based on PR and TMI observations of 20 MCS cases over diverse tropical land regions. The open circles in the plots denote observations from convective regions, while the filled circles represent observations from stratiform regions.

Figure 4: Average PR reflectivity, $\langle Z^* \rangle$, at different altitudes versus $\langle T85^* \rangle$ for **a)** convective and **b)** stratiform rain. The symbols denoting the various altitudes are shown as an inset in Panel b.

Figure 5: TMI scan pattern showing the centers of 85 GHz footprints; the beam effective field of view of the 19 GHz (see also Kummerow et al., 1998); and a 10 km Cb that is collocated with a 19 GHz fov . Also illustrated is the method to determine the location of a T85 minimum, $T85_{min}$, and the mean spatial gradient, $\overline{\left| dT85/dr \right|}$, around this minimum.

Figure 6: Plot of PR rain rate ($mmhr^{-1}$) averaged in discrete bins of 2 K for (T19-T37) and 5 K for T85, utilizing the TMI and PR data from 20 MCS cases over diverse tropical land regions.

Figure Captions (Continued)

Figure 7: Scatter plot of large-scale, area-averaged rain rates R_{PR}^A versus R_{Cb}^A and R_{V5}^A for the Amazon $5^\circ \times 5^\circ$ region (see text for details). The correlation between R_{PR}^A and R_{Cb}^A is 0.78, while it is 0.70 between R_{PR}^A and R_{V5}^A .

Figure 8: Scatter plots of **a)** R_{PR}^* versus R_{Cb}^* , and **b)** R_{PR}^* versus R_{V5}^* for the Amazon $5^\circ \times 5^\circ$ region. Note, R_{PR}^* , R_{Cb}^* , and R_{V5}^* represent averages over 19 GHz footprints.

Figure 9: Rain patterns given by the **a)** PR, **b)** TMI-Cb Algorithm, and **c)** TMI-V5 Algorithm for a TRMM satellite overpass of the Amazon $5^\circ \times 5^\circ$ region that occurred on 8 December 2000 (orbit number 17446).

Table Captions

Table 1: Average of PR and TMI data within a given 20 K interval of T_{85}^* for **a)** convective and **b)** stratiform rain. These averages are: $\langle T_{19} \rangle$, $\langle T_{37}^* \rangle$, $\langle T_{85}^* \rangle$, $\langle R^* \rangle$ and $\langle Z^* \rangle$. Also, convective and stratiform rain fractions are given. Note that $\langle Z^* \rangle$ is given for 1, 3, 4, 4.5, 6, 7, 9, and 11 km altitudes. The number of observations in a given T_{85} interval is also shown in these tables. The observations used to generate these statistics associated with convective and stratiform rain is deduced from 20 MCS cases over land regions.

Table 2: For 1) Strong Cbs ($\overline{dT_{85}/dr} > 1 \text{ Kkm}^{-1}$), 2) Weak Cbs ($0 < \overline{dT_{85}/dr} \leq 1 \text{ Kkm}^{-1}$), and 3) Areas Outside of Cbs inferred from TMI data: PR observed convective and stratiform rain fractions and rain rates, $\overline{R^*}$; and TMI observed $\overline{T_{85}^*}$ and $\overline{T_{19} - T_{37}^*}$.

Table 3: Values of the constants used in Eqs. 2, 4, and 5.

Table 4: List of $5^\circ \times 5^\circ$ land regions and the time periods used in our analysis.

Table 5: Correlation between PR rain rate and rain rates retrieved from the TMI-Cb and TMI-V5 Algorithms. **a)** Correlation on the large scale ($\leq 220 \times 550 \text{ km}^2$). **b)** Correlation on the scale of the 19 GHz *fov* ($\sim 18 \times 30 \text{ km}^2$).